Identifying hyperelastic constitutive parameters with sensitivity-based virtual fields

Adel Tayeb, Jean-Benoit Le Cam, Michel Grediac, Evelyne Toussaint, Eric Robin, Xavier Balandraud, Frederic Canevet

▶ **To cite this version:**

Adel Tayeb, Jean-Benoit Le Cam, Michel Grediac, Evelyne Toussaint, Eric Robin, et al.. Identifying hyperelastic constitutive parameters with sensitivity-based virtual fields. Strain, 2021, 57 (6), pp.e12397. 10.1111/str.12397 . hal-03330336

HAL Id: hal-03330336
https://hal.science/hal-03330336v1

Submitted on 2 Jun 2022

HAL is a multi-disciplinary open access archive for the deposit and dissemination of scientific research documents, whether they are published or not. The documents may come from teaching and research institutions in France or abroad, or from public or private research centers.

L'archive ouverte pluridisciplinaire **HAL**, est destinée au dépôt et à la diffusion de documents scientifiques de niveau recherche, publiés ou non, émanant des établissements d'enseignement et de recherche français ou étrangers, des laboratoires publics ou privés.

Distributed under a Creative Commons Attribution - NonCommercial 4.0 International License

Identifying hyperelastic constitutive parameters with sensitivity-based virtual fields

Adel Tayeb[1] | Jean-Benoît Le Cam*[1] | Michel Grédiac[2] | Evelyne Toussaint[2] | Eric Robin[1] | Xavier Balandraud[2] | Frédéric Canevet[3]

[1]Univ Rennes, CNRS, IPR (Institut de Physique de Rennes) - UMR 6251Rennes, France
[2]Université Clermont Auvergne, CNRS, SIGMA Clermont, Institut Pascal, 63000 Clermont-Ferrand, France
[3]Cooper Standard France, 194 route de Lorient, 35043 , Rennes, France

Correspondence
*Jean-Benoît Le Cam, Univ Rennes, CNRS, IPR (Institut de Physique de Rennes) - UMR 6251, Rennes, France. Email: jean-benoit.lecam@univ-rennes1.fr

Summary

This work deals with the identification of hyperelastic constitutive parameters using the virtual fields method. The choice of the virtual displacement fields is a cru-cial aspect of the method, typically for reducing the sensitivity to the measurement noise. A first and simple option is to generate the virtual displacement fields ran-domly. Nevertheless, in case of hyperelastic models for which the stress is not a linear function of the constitutive parameters, improving the choice of the virtual displace-ment fields is not trivial and an alternative strategy has to be found. In the present study, the sensitivity-based virtual fields approach is applied and compared to the randomly-generated virtual displacement fields approach. Two material models were considered: the Mooney model, which describes quite well the behavior of hyperelas-tic materials for small and moderate strains, and the Ogden model, which accounts for the stress hardening phenomenon observed at higher strains. The full kinematic fields are measured by using the digital image correlation technique during an equibiaxial tensile test performed on a cruciform specimen. Identification results are discussed through their capability to predict the external force measured during the test. The sensitivity-based virtual fields approach is found to improve significantly the predic-tion compared to the randomly-generated virtual displacement fields approach.

KEYWORDS:
Sensitivity-based virtual fields, identification, hyperelastic materials, full-field measurements

1 | INTRODUCTION

The characterization of the mechanical behavior of rubber materials is classically carried out within the framework of hyperelasticity [14]. In this representation, the behavior describes only rate-independent effects without hysteresis, with the assumption of isotropy and incompressibility. In this case, the constitutive parameters depend upon the loading conditions applied in the identification procedure [13]. This is the reason why they are generally identified from three homogeneous tests, namely the uniaxial tension (UT), the pure shear (PS) and the equibiaxial tension (EQT) [1]. An alternative approach consists in performing only one heterogeneous test in which the three loading states (UT, PS and EQT) are present along with various intermediate states. Moreover, the values of the identified parameters are unique for each heterogeneous test, see [12] and [25]. Several approaches have been developed for the identification of constitutive parameters from experimental heterogeneous tests such as the finite

[1]It should be noted that the EQT can be compared to the uniaxial compression (UC) [28]

element model updating technique, the equilibrium gap method or the virtual fields method, see [1] and [2] for further details. The latter method was applied before in the case of hyperelastic models and gave promising results, see [25]. This is the reason why it will be used in this work for the identification of hyperelastic constitutive parameters.

The Virtual Fields Method (*VFM*) was first introduced in [9] for the identification of constitutive parameters of linear elastic materials. It was applied over the years to several types of material behaviors. Within the framework of the small strain assumption, the method was used to characterize orthotropic materials in [8], [5] and [10], and elasto-plastic materials in [7] and [3], among others. Dynamic properties were studied in [6] for instance. In the recent past, the *VFM* was extended to the finite strain framework. From a historical point of view, the first application of the *VFM* for hyperelastic materials was presented in [25]. Mooney [19] and Yeoh [31] models were considered using a biaxial tensile test of a 4-branch cruciform specimen in a moderate strain range. Other hyperelastic models such as the Ogden model [22] was employed in [23] using a planar tension tests on a flat rubber specimen subjected to the same moderate strain range as in the previous reference. Furthermore, in addition to hyperelastic parameters, the *VFM* was used for the determination of viscoelastic properties of rubber, see [33] and [32], where dynamic tests were exploited for the identification.

This extensive use of the *VFM* for different mechanical behaviors and applications rose the challenge of the best choice of the virtual displacement fields, which is a crucial aspect of the method. Several techniques were used for addressing this problem when dealing with hyperelastic materials. In general, the virtual displacement fields are either chosen to cancel the actual loading term in the equation of the virtual work equation, see [33] and [32], or randomly, with a criterion on the conditioning of the linear system arising from the *VFM* [25]. In a recent work, a new procedure in the choice of independent virtual displacement fields has been introduced in the case of anisotropic plasticity with small deformations [17]. The method is based on the sensitivity of the stress field to changes of the constitutive parameters. The virtual displacement fields are then computed proportional to the stress sensitivity fields. This method was extended to finite strains in [18].

In the present work, the *VFM* is applied to the identification of hyperelastic constitutive parameters from an equibiaxial experiment performed with a 4-branch cruciform shaped specimen. Two strategies in the generation of the virtual displacement fields are applied and compared. First, the random virtual displacement fields strategy that was applied to the Mooney and the Yeoh models in [25], is extended to the Ogden model. Contrary to the former ones, the Ogden model leads to a non-linear stress relationship with respect to the constitutive parameters. This property makes it challenging to choose the best virtual displacement fields generated randomly. To overcome this issue, the sensitivity-based virtual displacement fields strategy has been developed within the framework of hyperelasticity by using the Mooney and Ogden models. This is the main contribution of the paper.

The paper is organized as follows. In the first section, the theoretical background of the *VFM* is recalled and the identification problem is formulated for the two hyperelastic models under consideration. The second section is devoted to the experimental setup, including the mechanical test and the digital image correlation technique. In the third section, the results of the identification procedure are discussed in terms of virtual displacement fields to be used in the identification procedure and the ability of the obtained parameters to accurately predict the external force applied during the test. In the final section, the sensitivity-based virtual fields method is applied to four different hyperelastic materials. Concluding remarks close the paper.

2 | THEORETICAL BACKGROUND

In this section, a literature survey is proposed about the use of the *VFM* for the identification of hyperelastic constitutive parameters. First, the basics of the method are recalled. Then the randomly-generated and sensitivity-based virtual displacement fields strategies are presented. Finally, the minimization problem arising from the application of the method is detailed. The Mooney [19] and Ogden [22] models are used for this purpose.

2.1 | Virtual fields method

Considering a hyperelastic solid subjected to a quasi-static loading and assuming that the volume forces can be neglected, the principle of virtual work, can be written as follows

$$-\int_V \boldsymbol{\sigma}(\boldsymbol{x},t) : \boldsymbol{\varepsilon}^*(\boldsymbol{x},t)\, dV + \int_{\partial V} \boldsymbol{T}\cdot\boldsymbol{u}^*(\boldsymbol{x},t)\, dS = 0, \tag{1}$$

where V is the volume of the solid, $\boldsymbol{\sigma}$ is the Cauchy stress tensor, $\boldsymbol{u}^*$ and $\boldsymbol{\varepsilon}^*$ are the virtual displacement and strain, respectively. $\boldsymbol{T}$ is the external force per unit deformed area. In general, the stress, virtual strain and displacement fields are all heterogeneous

fields at any time t. The stress field $\boldsymbol{\sigma}$ can be deduced from the measured displacement or strain fields by using the corresponding constitutive equations and a given set of material parameters. The virtual displacement $\boldsymbol{u}^*$ is a continuous function, which is kinematically admissible in the volume V. A sufficient condition regarding the admissibility of the virtual displacement field is to consider a continuous function, which satisfies the boundary conditions, (see [24]). The virtual strain field is deduced by using the strain-displacement relationship, namely $\boldsymbol{\varepsilon}^* = 1/2\left(\nabla \mathbf{u}^* + \nabla \mathbf{u}^{*T}\right)$. It should be noted that these two functions are also called *test functions* or *weighting functions*. They are completely independent from the real strain and displacement fields. In Eq. (1), the first integral is the contribution of the internal virtual work due to deformations. The second integral accounts for the contribution of the external loading applied to the solid. Given that most full-field measurement techniques provide information on the specimen's surface, a two dimensional problem should be considered. Typically, a plane stress problem is considered in the case of thin specimen. Under this assumption, Eq. (1) becomes

$$-e\int_S \boldsymbol{\sigma}(x,y,t) : \boldsymbol{\varepsilon}^*(x,y,t)\, dS + e\int_{\partial S} \boldsymbol{T}\cdot\boldsymbol{u}^*(x,y,t)\, dL = 0, \tag{2}$$

where e is the thickness of the solid, S is the surface of the solid in the normal direction to the thin dimension and ∂S is its boundary.

Full-field measurements, especially when performed with digital image correlation are based on the decomposition of the surface of the specimen into a set of subsets. The displacement at the centre of these zones is then deduced by minimizing the optical residual (see [4] and [30]). The displacement, strain and stress fields are discrete functions, which are evaluated only at these discrete points. The internal virtual work part of Eq. (1) becomes

$$e\left(\sum_{i=1}^{nPts}\left(\boldsymbol{\sigma}^i\cdot\boldsymbol{\varepsilon}^{*i}\right)S^i\right), \tag{3}$$

where $nPts$ is the number of data points in the region of interest ROI. $\boldsymbol{\sigma}^i$, $\boldsymbol{\varepsilon}^{*i}$ and S^i are the stress, virtual strain and area surrounding each data point, respectively. The external virtual work contribution is computed using the second integral of Eq. (1). Given that only the resulting force and not its distribution is measured along the edge of the specimen ∂S, two methods can be used for calculating this part of the virtual work. The first one consists in considering a constant virtual displacement along the edge. The contribution is then obtained by multiplying the resulting force by the constant virtual displacement. The second method consists in assuming a uniform force distribution along the edge and using a non-constant virtual displacement. The product between these two quantities is then integrated over ∂S.

The stress in Eq. (3) is a function of the set of constitutive parameters to be identified. This set is denoted here by $\boldsymbol{\chi}$, and the strain by $\boldsymbol{\varepsilon}$. The *VFM* is based on the application of the principle of virtual work and on the minimization of the difference between internal and external virtual works. For materials with linear dependency of the stress upon the constitutive parameters, the principle of virtual work is applied at least as many times as the number of constitutive parameters contained in $\boldsymbol{\chi}$. In this case, such as for linear elastic materials, this minimization leads to a linear system which gives the constitutive parameters after inversion. However, for other models such as those used with elasto-plastic materials, for which the stress is nonlinear with respect to the constitutive parameters, a nonlinear least-square minimization procedure must be employed. One or several specimen strain levels are used in the minimization. Two forms of the cost-function are proposed accordingly:

$$\boldsymbol{f}(\boldsymbol{\chi},\boldsymbol{\varepsilon}) = \sum_{j=1}^{nVF}\left(\sum_{i=1}^{nPts}\left(\boldsymbol{\sigma}^i(\boldsymbol{\chi},\boldsymbol{\varepsilon})\cdot\boldsymbol{\varepsilon}^{*i(j)}\right)S^i - W_{ext}^{*j}\right)^2, \tag{4}$$

for one specimen strain level and

$$\boldsymbol{f}(\boldsymbol{\chi},\boldsymbol{\varepsilon}) = \sum_{j=1}^{nVF}\left[\sum_{t=1}^{nTime}\left(\sum_{i=1}^{nPts}\left(\boldsymbol{\sigma}^i(\boldsymbol{\chi},\boldsymbol{\varepsilon},t)\cdot\boldsymbol{\varepsilon}^{*i(j)}(t)\right)S^i - W_{ext}^{*(j)}(t)\right)^2\right], \tag{5}$$

for several specimen strain levels. In Eqs. (4) and (5), nVF and $nTime$ represent the number of independent virtual fields and time steps, respectively.

To apply this method to hyperelastic materials, Eqs. (1) to (5) should be expressed in the finite strain framework. As in [25] and [24] among others, the principle of virtual work is expressed as a function of the first Piola-Kirchhoff stress tensor $\boldsymbol{\Pi}$, which

represents the current force per unit of undeformed area. In this case, the principle of virtual work can be expressed as follows

$$-E\int_{S_0}\boldsymbol{\Pi}(\boldsymbol{X},t):\frac{\partial \boldsymbol{U}^*}{\partial \boldsymbol{X}}(\boldsymbol{X},t)\,dS_0+E\int_{\partial S_0}(\boldsymbol{\Pi}\cdot\boldsymbol{N})\cdot\boldsymbol{U}^*(\boldsymbol{X},t)\,dL_0=0, \tag{6}$$

where subscript $\bullet_0$, $\boldsymbol{X}$, E and $\boldsymbol{N}$ designate quantities given in the reference configuration [2], the coordinates, the thickness and the vector normal to the edge in the same configuration, respectively. Eqs. (4) and (5) become

$$\boldsymbol{f}(\chi)=\sum_{j=1}^{nVF}\left(\sum_{i=1}^{nPts}\left(\boldsymbol{\Pi}^i(\chi)\cdot\frac{\partial \boldsymbol{U}^{*i(j)}}{\partial \boldsymbol{X}}(\boldsymbol{X})\right)S^i-W_{ext}^{*(j)}\right)^2, \tag{7}$$

when considering one specimen strain level and

$$\boldsymbol{f}(\chi)=\sum_{j=1}^{nVF}\left[\sum_{t=1}^{nTime}\left(\sum_{i=1}^{nPts}\left(\boldsymbol{\Pi}^i(\chi,t)\cdot\frac{\partial \boldsymbol{U}^{*i(j)}}{\partial \boldsymbol{X}}(\boldsymbol{X},t)\right)S^i-W_{ext}^{*(j)}(t)\right)^2\right], \tag{8}$$

when considering several specimen strain levels. The identification of the constitutive parameters is carried out by using the *fminsearch* function of Matlab for nonlinear models, and by inverting the linear system for linear models. It should be noted that this function can lead to a local minimum. This issue was tracked by reconstructing the force-displacement curve with set of identified parameters. Indeed, curves plotted with parameters extracted from local minima are not in good agreement with the experimental one. In this case, these parameters are discarded and a new identification is performed with different initial values. The procedure can be repeated until a good agreement between the curves is obtained. Note that in all the cases reported here, launching the procedure once was sufficient. Further details on the procedure are presented in the remainder of this section.

2.2 | Hyperelasticity

The mechanical behavior of elastomers is generally described within the framework of hyperelasticity. The stress is obtained by deriving the strain energy density W with respect to the corresponding strain measure. This strain energy density relates the stress to the strain through the principal stretches or the principal invariants of the Cauchy-Green strain tensors. In the following, the material is assumed to be incompressible. Under this assumption, the first Piola-Kirchhoff stress tensor is given by

$$\boldsymbol{\Pi}=-p\boldsymbol{F}^{-t}+\frac{\partial W}{\partial \boldsymbol{F}}, \tag{9}$$

where p is a Lagrange multiplier due to incompressibility (see [29]), $\boldsymbol{F}$ is the deformation gradient tensor and $\bullet^t$ designates the transpose of a second-order tensor. For the Mooney model [19], the strain energy density reads as follows

$$W=c_1\left(I_1-3\right)+c_2\left(I_2-3\right), \tag{10}$$

where I_1 and I_2 are the first and second invariants of the right Cauchy-Green strain tensor, respectively. c_1 and c_2 are the constitutive parameters to be identified. Combining Eqs. (9) and (10) and replacing $\boldsymbol{\Pi}$ by its expression in Eq. (6) lead to the following expression of the principle of virtual work for this material

$$c_1\int_{S_0}\boldsymbol{\Theta}:\frac{\partial \boldsymbol{U}^*}{\partial \boldsymbol{X}}dS_0+c_2\int_{S_0}\boldsymbol{\Lambda}:\frac{\partial \boldsymbol{U}^*}{\partial \boldsymbol{X}}dS_0=\int_{\partial S_0}(\boldsymbol{\Pi}\cdot\boldsymbol{N})\cdot\boldsymbol{U}^*dL_0, \tag{11}$$

where $\boldsymbol{\Theta}$ and $\boldsymbol{\Lambda}$ are two functions of the principle stretches defined in Appendix A. Using Eq. (11) with two independent virtual displacement fields leads to the following system

$$\begin{aligned}&\boldsymbol{Ac}=\boldsymbol{B}\\&\text{with}\\&\boldsymbol{A}=\begin{bmatrix}\int_{S_0}\boldsymbol{\Theta}:\frac{\partial \boldsymbol{U}^{*(1)}}{\partial \boldsymbol{X}}dS_0 & \int_{S_0}\boldsymbol{\Lambda}:\frac{\partial \boldsymbol{U}^{*(1)}}{\partial \boldsymbol{X}}dS_0\\ \int_{S_0}\boldsymbol{\Theta}:\frac{\partial \boldsymbol{U}^{*(2)}}{\partial \boldsymbol{X}}dS_0 & \int_{S_0}\boldsymbol{\Lambda}:\frac{\partial \boldsymbol{U}^{*(2)}}{\partial \boldsymbol{X}}dS_0\end{bmatrix}\\&\boldsymbol{c}=\begin{Bmatrix}c_1\\c_2\end{Bmatrix}\quad\text{and}\quad\boldsymbol{B}=\begin{Bmatrix}\int_{\partial S_0}(\boldsymbol{\Pi}\cdot\boldsymbol{N})\cdot\boldsymbol{U}^{*(1)}dL_0\\ \int_{\partial S_0}(\boldsymbol{\Pi}\cdot\boldsymbol{N})\cdot\boldsymbol{U}^{*(2)}dL_0\end{Bmatrix}\end{aligned}. \tag{12}$$

[2] chosen here to be the undeformed configuration

This linear system gives the two constitutive parameters c_1 and c_2 after inversion. The second model considered in this work is the Ogden model [22] for which the strain energy density is expressed by the following quantity

$$W = \sum_{i=1}^{N} \frac{2\mu_i}{\alpha_i^2} \left(\lambda_1^{\alpha_i} + \lambda_2^{\alpha_i} + \lambda_3^{\alpha_i} - 3 \right), \tag{13}$$

where λ_1, λ_2 and λ_3 are the principal stretches and μ_i, α_i; $i = 1..N$ are the constitutive parameters to be identified. The stretch λ is defined as the ratio between the current and the initial length in a given direction. Note that expressing the strain energy density with respect to the principal stretches implies that all tensors are expressed in the principal basis of the strain tensor. Hence, the first step is to determine the principal basis for each data point, and then to express the displacement and strain fields in these bases. From Eqs. (9) and (13) the eigenvalues of the Piola-Kirchhoff stress tensor are given by

$$\Pi_i = \frac{\partial W}{\partial \lambda_i} - \lambda_i^{-1} p. \tag{14}$$

The indeterminate coefficient p is identified assuming a plane stress state ($\Pi_3 = 0$). Replacing Π_i in the principle of virtual work leads to the following equation

$$-\int_{S_0} \left(\Pi_1 \cdot U^*_{u,u} + \Pi_2 \cdot U^*_{v,v} \right) dS_0 + \int_{\partial S_0} (\boldsymbol{\Pi} \cdot \boldsymbol{N}) \cdot \boldsymbol{U}^* (\boldsymbol{X}, t)\, dL_0 = 0, \tag{15}$$

where (u, v) is the principal basis for the strains. In this basis, the cost function defined in Eq. (8) becomes

$$\boldsymbol{f}(\chi) = \sum_{j=1}^{nVF} \left[\sum_{t=1}^{nTime} \left(\sum_{i=1}^{nPts} \left(\Pi_1(\chi) \cdot U^{*i(j)}_{u,u} + \Pi_2(\chi) \cdot U^{*i(j)}_{v,v} \right) S^i - W^{*(j)}_{ext} \right)^2 \right]. \tag{16}$$

In this work, two orders were considered for the Ogden model, namely are the first and the second orders. The identification of the constitutive parameters was performed by minimizing the cost function $\boldsymbol{f}$. At least 2 or 4 independent virtual displacement fields were used in the identification procedure for the first and second order Ogden models, respectively. It should be noted, however, that only the second-order Ogden model satisfactorily describes the stress-hardening phenomenon observed in the stress-strain curves.

2.3 | Choice of the virtual displacement fields

There is an infinite number of virtual fields $\boldsymbol{U}^*$ that satisfy the principle of virtual work in Eq. (6). The choice of a set of independent virtual fields remains a critical issue. A first attempt was to consider arbitrary expressions for the virtual fields defined over the whole specimen. Examples are available for isotropic and anisotropic elastic materials, see [11], [24] and [10]. Piecewise displacement virtual fields were also used in [27]. In the case of hyperelasticity, virtual displacement fields can be chosen randomly. This option is detailed in section 2.3.1. In the present work, the sensitivity-based virtual displacement fields strategy introduced in [17] is extended to hyperelasticity. It is presented in section 2.3.2. It should be noted that the hyperelastic model has a significant effect on these strategies and their robustness. This point is addressed in what follows.

2.3.1 | Randomly-generated virtual displacement fields

To the best of the authors' knowledge, the *VFM* was firstly applied for hyperelastic materials in [25]. Motivated by a noise-sensitivity reduction, a set of randomly-generated virtual displacement fields was used. The procedure used in [25] relies on the division of the (*ROI*) into several quadrangular sub-domains, and on the generation of random values for the virtual displacements at the nodes of these sub-domains. Then, the displacement is interpolated in the whole domain using four-noded quadrangular finite element formulations [34]. These displacement fields take the following expressions as functions of the nodal virtual displacements

$$\begin{aligned} \boldsymbol{U}^*_x &= \sum_{k=1}^{4} N_k(\xi, \eta)\, U_x^{*(k)} \\ \boldsymbol{U}^*_y &= \sum_{k=1}^{4} N_k(\xi, \eta)\, U_y^{*(k)} \end{aligned}, \tag{17}$$

where N_k are the shape functions, ξ and η are the coordinates in the reference element. These displacements are given in the reference element coordinate system (ξ, η). They should therefore be given in the global coordinate system (x, y). This is

achieved by defining the transformation between these two coordinate systems. Note that in the case of a regular element grid, this transformation may be omitted and the global coordinate system (x, y) can be used in Eq. 17. In [25], the randomly-generated virtual displacement fields were used for the Mooney [19] and the Yeoh [31] hyperelastic models, for which the application of the *VFM* leads to a linear system. In this case, to ensure the independence of the virtual fields, a good conditioning of the linear system (12) must be obtained. However, for models for which the *VFM* does not lead to a linear system such as the Ogden model, no criterion was found to generate independent virtual fields with this approach.

2.3.2 | Sensitivity-based virtual displacement fields

In a recent work [17], a new procedure for generating independent virtual displacement fields was employed for the identification of the constitutive parameters of an anisotropic plastic model in the small strain domain. The method is based on the sensitivity of the stress to changes of the constitutive parameters, typically between 10 and 20 %. The virtual displacement fields are then generated proportionally to the stress sensitivity fields by using an approach inspired from the finite element formulation. These stress sensitivity fields being computed from time-dependent strain fields, the former are time dependent as well as their corresponding virtual displacement fields.The method was then extended to the finite strain domain in [18] for anisotropic plasticity. In the finite strain domain, the stress sensitivity field is defined by

$$\delta\boldsymbol{\Pi}^{(i)}(\chi,t) = \boldsymbol{\Pi}\left(\chi + \delta\chi_i, t\right) - \boldsymbol{\Pi}(\chi,t), \tag{18}$$

where $0.1\ \chi_i \leq \delta\chi_i \leq 0.2\ \chi_i$ is the range of variation of the i^{th} parameter from a mean value $\bar{\chi}_i$ obtained from a literature survey. Note that the stress sensitivity of Eq. (18) gives the influence of each constitutive parameter to the global response of the material at each point since the stress field is heterogeneous for this experiment. The virtual displacement fields were related to the stress sensitivity fields by the relation inspired from the finite element formulation, which gives

$$\delta\boldsymbol{\Pi}^{(i)}(\chi,t) = \boldsymbol{B}_{glob}\boldsymbol{U}^{*(i)}(t), \tag{19}$$

where $\boldsymbol{B}_{glob}$ is the global strain-displacement matrix obtained from a virtual mesh generated a priori. This matrix is obtained from the assembly of the elementary strain-displacement matrix obtained directly from the differentiation of the shape functions in Eq. (17) with respect to the coordinates in the (x, y) plane. $\boldsymbol{U}^{*(i)}$ in Eq. (19) designates the virtual displacement field corresponding to the i^{th} constitutive parameter. It is worth remembering that this displacement field is a *test function*, which is not related to the actual displacement field. In practice, matrix $\boldsymbol{B}_{glob}$ should be modified to account for the boundary conditions of the *ROI*. Typically, for edges where the external loading is unknown, a null displacement should be imposed to account for this constraint. A new matrix $\bar{\boldsymbol{B}}_{glob}$ is therefore obtained from the original matrix $\boldsymbol{B}_{glob}$. The virtual displacement field is then expressed as follows

$$\boldsymbol{U}^{*(i)}(t) = pinv\left(\bar{\boldsymbol{B}}_{glob}\right)\delta\boldsymbol{\Pi}^{(i)}(\chi,t), \tag{20}$$

where *pinv* designates the pseudo inverse operator. Once the virtual displacement field is obtained, its gradient involved in the virtual work principle is deduced by using the following classic relationship inspired from the finite element method

$$\frac{\partial\boldsymbol{U}^{*(i)}(t)}{\partial\boldsymbol{X}} = \boldsymbol{B}_{glob}\boldsymbol{U}^{*(i)}(t). \tag{21}$$

The contribution of each constitutive parameter to the response of the material is specific and may be very different in magnitude. A scaling in the cost function should therefore be added, see [17] and [18]. Eqs. (7) and (8) become

$$\boldsymbol{f}(\chi) = \sum_{j=1}^{nVF}\left(\frac{1}{\left(\alpha^{(j)}\right)^2}\sum_{i=1}^{nPts}\left(\boldsymbol{\Pi}^i(\chi)\cdot\frac{\partial\boldsymbol{U}^{*i(j)}}{\partial\boldsymbol{X}}(\boldsymbol{X},t)\right)S^i - W_{ext}^{*(j)}\right)^2, \tag{22}$$

when one specimen strain level is considered and

$$\boldsymbol{f}(\chi) = \sum_{j=1}^{nVF}\left[\frac{1}{\left(\alpha^{(j)}\right)^2}\sum_{t=1}^{nTime}\left(\sum_{i=1}^{nPts}\left(\boldsymbol{\Pi}^i(\chi,t)\cdot\frac{\partial\boldsymbol{U}^{*i(j)}}{\partial\boldsymbol{X}}(\boldsymbol{X},t)\right)S^i - W_{ext}^{*(j)}(t)\right)^2\right], \tag{23}$$

when several specimen strain levels are considered. In Eqs.(22) and (23), $\alpha^{(j)}$ denotes the mean internal virtual work *IVW* obtained from the virtual fields corresponding to the j^{th} parameter, which is expressed as follows

$$IVW^{(j)}(t) = \sum_{i=1}^{nPts}\left(\boldsymbol{\Pi}^i(\chi,t)\cdot\frac{\partial\boldsymbol{U}^{*i(j)}}{\partial\boldsymbol{X}}(\boldsymbol{X},t)\right)S^i. \tag{24}$$

In Eq. (24), the first Piola-Kirchhoff stress tensor $\mathbf{\Pi}$ is evaluated by using the set of reference values for the constitutive parameters. In the identification procedure, the number of images considered (i.e. $nTime$) strongly depends on the dependence of the stress upon the constitutive parameters. In general, a large distribution of the global stretch λ_{glob} is needed in order to successfully perform the identification. Therefore, a heterogeneous experiment is needed.

3 | EXPERIMENTS

The aim of this section is to present the experimental setup and to briefly recall the main characteristics of the DIC measurement system used in this study.

3.1 | Material and specimen geometry

The material used in this study is a carbon black filled natural rubber. The specimen is shown in Figure 1. It is a 105 *mm* long and 2 *mm* thick cruciform specimen with 6 *mm* cylindrical ends to avoid slippage in the testing machine grips. A similar specimen geometry was firstly used in [25] for the characterization of natural rubber. This specimen shape gives various states of strain when an equibiaxial load is applied. The classic states presented previously, namely the UT, the PS and the EQT, are induced as well as various intermediate states of strain. Therefore, the single heterogeneous test used in this study provides an interesting alternative to these multiple homogeneous tests classically used for the identification of hyperelastic constitutive parameters. This procedure gives a complete response of the specimen for the various strain states obtained with a wide distribution of the biaxiality coefficient.

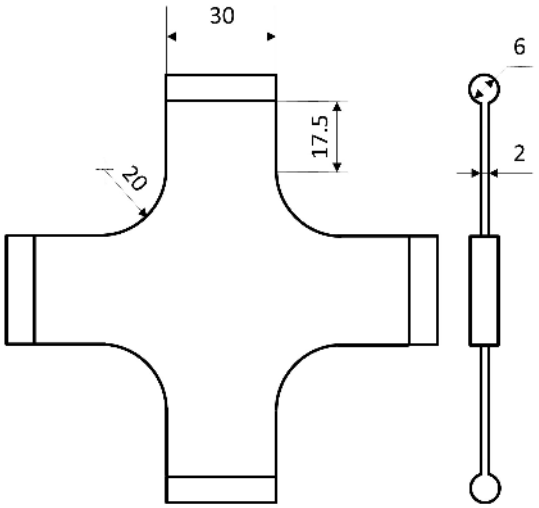

Figure 1 Specimen geometry (dimensions in *mm*)

3.2 | Loading conditions

The experimental setup is presented in Figure 2. It is composed by a home-made biaxial testing machine and a digital camera. The machine is formed by four independent RCP4-RA6C-I-56P-4-300-P3-M (IAI) electrical actuators controlled by PCON-CA-56P-I-PLP-2-0 controller and four PCON-CA (IAI) position controllers. All these components are controlled by an in-house LabVIEW program. The biaxial testing machine is equipped with two cell loads with a capacity of 1094 N, which store the force variation in the two perpendicular directions. In this work, an equibiaxial load was applied to the cruciform specimen. The four independent actuators were linked to have the same movement. This movement is such that the specimen center was motionless during the test. Hence, a reference point was obtained at the center of the specimen with respect to the correlation procedure. A displacement of 70 mm was applied to each branch at a loading rate of 150 mm/min for five cycles. This choice was made in order to identify the stabilized behavior of the specimen since the material accommodates during the first cycles [20]. The maximum applied displacement corresponds to a global stretch λ_{glob} [3] of 2.33.

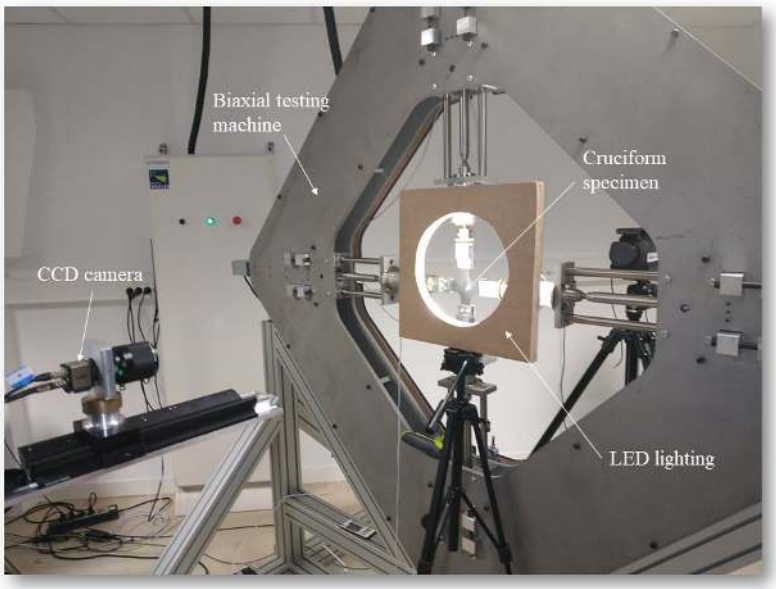

Figure 2 Experimental setup

3.3 | Full-field kinematic measurement

During the mechanical test, images of the specimen surface were stored at a frequency of 5 Hz using an IDS camera equipped with a 55 mm telecentric objective. The charge-coupled device (CCD) sensor of the camera has 1920×1200 joined pixels. The displacement field at the surface of the specimen was determined by using digital image correlation technique. It consists in correlating the grey levels between two different images of a given zone at two different levels of strain [26]. Before the test, the specimen was sprayed by a white paint in order to improve the image contrast. Hence, a black and white random grey field was obtained. During the test, the specimen was subjected to a uniform cold lighting thanks to a home-made LED lighting system. This ensures the uniform distribution of the lighting even at the highest strains reached. The correlation process was performed by the SeptD software [30], which is dedicated to both finite and small strain domains. Following the recommendation of the DIC guide [15], both DIC hardware and analysis parameters are given in tables 1 and 2 respectively. Note that the size of the subset in mm could vary from one test to another depending on the positioning of the camera and its parameters. Thanks to the symmetry of the test, a rectangular region on one branch of the specimen is sufficient to apply the identification procedure described in Section 2. This choice ensures a trade-off between:

[3] the ratio between the current and the initial lengths of the specimen in a given direction

- a large distribution of the loading cases within the *ROI*,
- a large strain level for each loading case,
- the convergence of the DIC calculation for the chosen *ROI* during the whole experiment, including the case of large strains.

The rectangular *ROI* is represented in Figure 3. It corresponds to a zone from the specimen center to the cylinder at the end of its branch. The gauge block shown in Fig. 3 is used for converting pixels to millimeters. The result of the correlation is

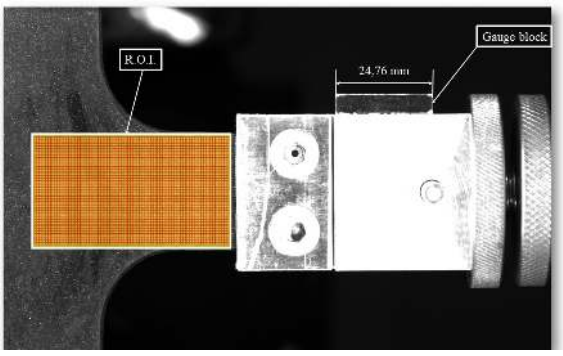

Figure 3 Region of interest with a 4 pixels step size

the displacement field over the *ROI* at each data point. Strain and displacement gradient tensors fields are then derived from these displacement fields. The displacement fields obtained from the correlation process were stored by the SeptD software as two matrices whose components correspond to each data point of the *ROI*. Due to the large displacement applied during the experiment, the correlation was not achieved in some subsets (less than 4% of the total number of subsets). The displacement in these subsets was approximated through a polynomial interpolation from all the subsets nearby. The displacement fields are then smoothed using a mean filter in order to reduce the experimental noise, especially where significant gradient occurred. This filter was applied before and after differentiation of the displacement fields in the computation of the displacement gradient tensor. Further details are given in Section 4.

Camera	IDS UI-3160CP Rev. 2
Image Resolution	1920 x 1200 pixels^2
Lens	55 mm C-mount partially telecentric.Constant magnification over a range of working distances ±12.5mm of object movement before 1% error image scale occurs
Aperture	f/5.6
Field-of-View	139.4 x 87.1 mm
Image Scale	14 pixels/mm
Stand-off Distance	1100 mm
Image Acquisition Rate	5 Hz
Patterning Technique	White spray on black specimen
Pattern Feature Size (Approximation)	6 pixels

Table 1 DIC Hardware parameters

DIC Software	7D©
Image Filtering	None
Subset Size	20 pixels/1.45 mm
Step Size	4 pixels/0.29 mm
Subset Shape Function	Affine
Matching Criterion	Normalized Cross Correlation
Interpolant	Bi-cubic
Strain Window	5 data points
Virtual Strain Gauge Size	36 pixels/ 2.62mm
Strain Formulation	Logarithmic
Post-Filtering of Strains	None
Displacement Noise-Floor	0.036 pixels/ 2.6 μm
Strain Noise-Floor	6.1 mm/m

Table 2 DIC Analysis parameters

4 | RESULTS

In this section, the results of the identification carried out with two procedures, namely the sensitivity-based and the randomly-generated virtual displacement fields strategies, are highlighted. A comparison between the force obtained experimentally and from finite element simulations using the identified constitutive parameters is used to assess the efficiency of each procedure.

4.1 | Experimental displacement fields

The displacement field obtained for a global stretch λ_{glob} of 2.33 with the SeptD software is given in Figure 4. Note that the dark blue zones in the two maps correspond to the subsets where correlation could not be successfully performed. Results of the displacement fields smoothed by the procedure described above are reported in Figure 5. The displacement gradient fields were obtained from the displacement fields by classic differentiation with respect to the spatial coordinates. First, the displacement fields were interpolated over the whole subset using the displacement of the four nodes defining the corners by the following expression

$$\begin{aligned} U_x(x,y) &= a \cdot x + b \cdot y + c \cdot x \cdot y + d \\ U_y(x,y) &= e \cdot x + f \cdot y + g \cdot x \cdot y + h \end{aligned}. \tag{25}$$

The displacement gradient tensor was then deduced from Eq. (25). Thus

$$\frac{\partial \boldsymbol{U}}{\partial \boldsymbol{X}} = \begin{bmatrix} a + c \cdot y & b + c \cdot x \\ e + g \cdot y & f + g \cdot x \end{bmatrix}. \tag{26}$$

Note that the eight constants $a \cdots h$ in Eqs. (25) and (26) are different from one subset to another. They are obtained by inverting the linear system of eight equations arising from Eq. (25). The displacement gradient fields are presented in Figure 6. These data were smoothed using the same filter as that used for the displacement fields. The distribution of the loading cases and the maximum principal stretches are reported in Figures 7(a) and 7(b), respectively. Fig. 7(a) highlights that the *ROI* chosen in this work contains a wide range of biaxiality coefficient defined by $\log\left(\lambda_{\min}/\lambda_{\max}\right)$. Indeed, it covers all loading cases lying between EQT and UT. Furthermore, a wide distribution of loading cases is observed in the *ROI* chosen (i.e. the points in the (I_1, I_2) plane cover a significant range). Figure 8 illustrates this distribution, in which both invariants I_1 and I_2 were plotted for the classic UT, PS and EQT loading cases, as well as for the present experimental results. Note that this distribution is given for the maximum applied displacement. For lowest applied displacements, the points in Fig. 8 are located from the origin of the (I_1, I_2) plane ($I_1 = I_2 = 3$) to the distribution corresponding to the maximum applied displacement. This means that the maximum principal stretch distribution is large enough whatever the loading case considered. The maximum value of the principal stretch reaches 3 in the UT zone for the maximum value of the displacement equal to 70 *mm*. This value is large enough for activating the stress hardening phenomenon. Among the models considered in this study, this phenomenon is only described by the second-order Ogden model. The other two models can be therefore suitable for describing the behavior of the material up to a strain level

corresponding to the occurrence of the stress hardening. The data obtained experimentally were used in the identification of the constitutive parameters for randomly-generated and sensitivity-based virtual displacement fields.

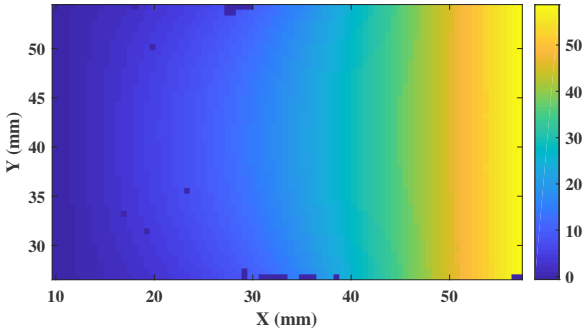

(a) Displacement field along X-direction U_x in *mm*

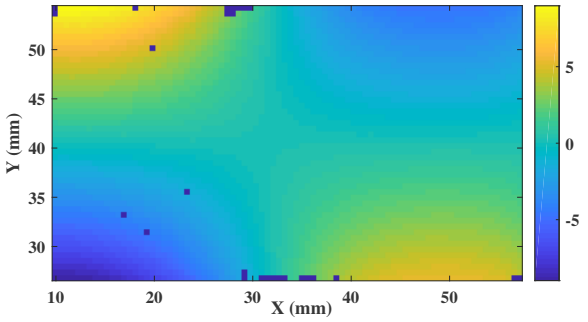

(b) Displacement field along Y-direction U_y in *mm*

Figure 4 Experimental displacement fields in the *ROI* for a global displacement of 70 *mm*

4.2 | Identification from randomly-generated virtual fields

The identification procedure described in section 2.3.1 was applied herein for the determination of the hyperelastic constitutive parameters. As described above, the virtual displacement was randomly generated at the nodes of the correlation grid (data points). Then, the virtual displacement field at any point was obtained by interpolating the nodal displacements. For the Mooney model, the virtual displacement fields were chosen in such a way that the conditioning of the matrix $\boldsymbol{A}$ in Eq. (12) was above 0.3. The two virtual displacement fields used in the identification of the Mooney parameters are presented. For the Ogden model, no criterion was found for the choice of the virtual displacement fields in Figure 9. Hence, a set of 100 virtual displacement fields was randomly generated and used in the identification procedure, (i.e. the 100 randomly-generated virtual displacement fields were used in the cost-function of Eq. 16). Note that for both models, the identification procedure was performed several times in order to obtain an objective criterion which could assess the efficiency of the method. Furthermore, the initial values for the fminsearch function (denoted x_0) were set to the reference (x_{ref}), minimum (x_{min}) and maximum (x_{max}) values reported

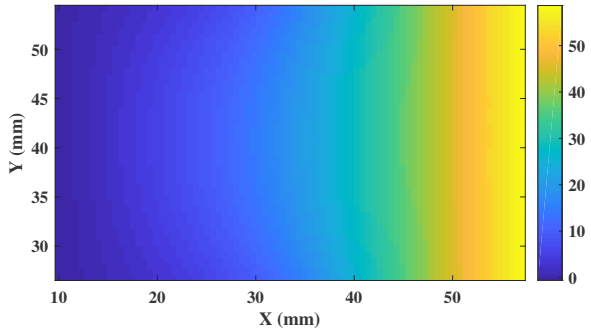

(a) Displacement field along X-direction U_x in mm

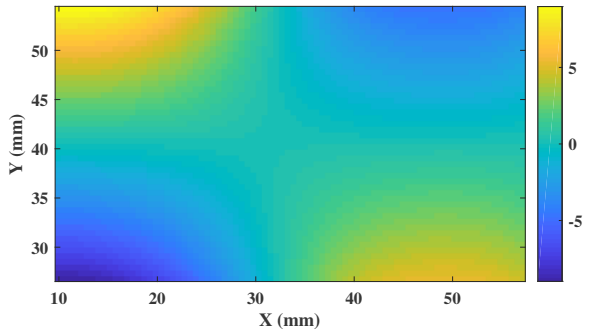

(b) Displacement field along Y-direction U_y in mm

Figure 5 Smoothed experimental displacement fields in the *ROI* for a global displacement of 70 *mm*

in Table 4. The parameters identified using this approach are reported in Table 3. The parameters for the three models appear to be in good agreement with the values found in the literature for natural rubber, (see [16]). However, no significant change on the ability of the identified parameters to predict the mechanical response has been found for this model. This is due to the non-linearity of the stress upon the constitutive parameters for this model which led to the lack of an objective criterion in the choice of the virtual fields. The final values of the objective function for the Ogden models were 0.42 and 0.20 for the first and second orders, respectively.

4.3 | Identification from sensitivity-based virtual fields

The identification procedure presented in section 2.3.2 was then used to obtain the hyperelastic constitutive parameters from the same test data. First, a virtual mesh had to be generated (it can be different from the correlation grid). Then, the virtual fields were generated proportionally to the stress sensitivity fields. The reference values for the parameters used in this work are given in Table 4. These values are found in the literature for similar materials, see [16]. As an example, the two virtual fields used with the Mooney model are shown in Figure 10, where $U^{*(1)}_{xc_1}, .., U^{*(2)}_{yc_2}$ designate the components of the two sensitivity-based virtual

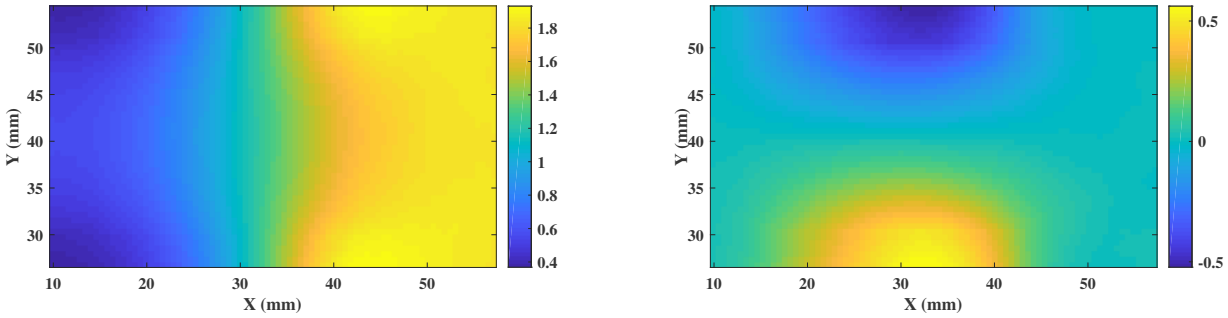

(a) $U_{x,x}$ (b) $U_{x,y}$

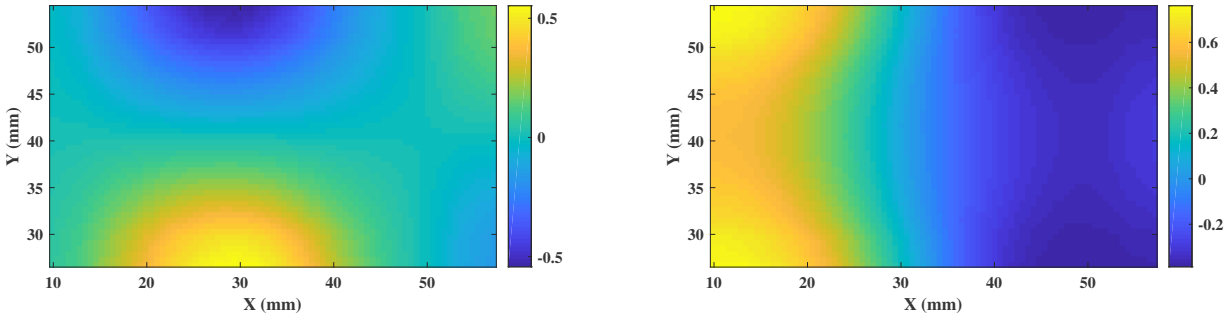

(c) $U_{y,x}$ (d) $U_{y,y}$

Figure 6 Displacement gradient fields obtained from Eq. (26)

displacement fields [4]. The values of the identified parameters are given in Table 5. Contrary to results obtained with randomly-generated virtual fields, the identified parameters for all the models considered are in good agreement with the reference values of a natural rubber. The identification took in average about 75 seconds for each model. Note that the parameters reported in Table 5 are obtained for several simulations with different sensitivity parameters, i.e. with different virtual fields. Furthermore, the mean parameter values used in the generation of the sensitivity-based virtual displacement fields do not affect the final result of the identification. In fact, the mean values for each parameter could change within the reference range without affecting the final result of the identification. For the Ogden model, the mean least squared error (the value of the objective function of Eq. 23 at the end of the identification procedure) is about 1.5 10^{-5} and 2.5 10^{-6} for the first and the second orders, respectively. This values are negligible compared to the ones obtained with randomly-generated virtual fields reported in the previous section.

4.4 | Comparison of the results

To evaluate the accuracy of the identified parameters, the biaxial experiment used in this work was simulated using Abaqus software for a plane stress problem using the parameters reported in Tables 3 and 5. The finite element model is presented in Figure 11. The element type used was the *CPS4* element, which is a four-noded bilinear plane stress quadrilateral. The four edges of the cruciform specimen were subjected to a tension displacement of 70 *mm* each. The displacement was blocked in

[4]These displacement fields are reported in Appendix A for the other two models.

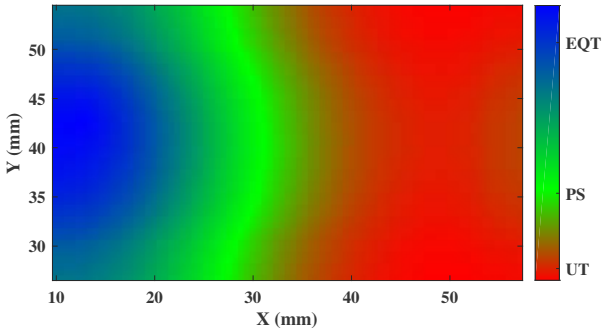

(a) Loading cases: **EQT**: equibiaxial tension; **PS**: pure shear; **UT**: uniaxial tension

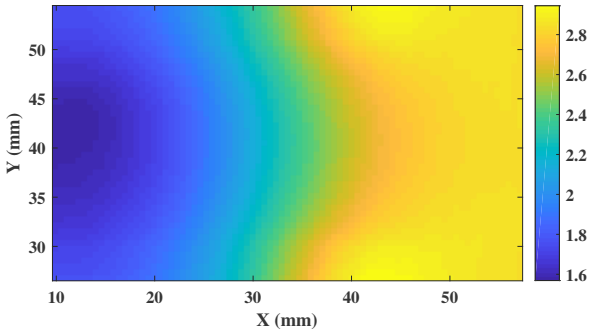

(b) Maximum principal stretches λ_{max}

Figure 7 Loading cases and maximum principal stretches for a global displacement of 70 *mm*

the transverse direction along the edges of the specimen. For each set of parameters, the resulting force in every branch was compared to the experimental force obtained during the experiment. It is worth noting that the force was measured in the two perpendicular directions. Since the loading was symmetric, only one load cell was used in each direction. The results of the comparison are shown in Figure 12, in which *SBVF* and *RVF* refer to sensitivity-based virtual fields and randomly-generated virtual fields, respectively. For the *RVF* method, the Mooney model appears to fairly predict the response for a global stretch up to 2, which is just before the inflection point of the force-displacement curve. This is the usual validity range for the Mooney model. On the other hand, both Ogden models either underestimated or overestimated the force in the branch for the whole test and the different initial values for the fminsearch function. This is due to the procedure for the choice of the virtual displacement fields, which were randomly generated in this case. With this approach, no criterion was found in their selection for the Ogden model. For the *SBVF* method, the Mooney model also correctly predicted the experimental force for a global stretch up to 2. Better results were obtained with the first-order Ogden model for a wider strain range, corresponding to a global stretch up to 2.15. The results given by these two models were very satisfactory since they do not take into account the stress hardening phenomenon. The second-order Ogden model predicts very well the experimental force for the whole test. Especially, the stress-hardening phenomenon, which is observed by the inflection point in the experimental force curve for a global stretch around 2.15. Such a result could not be obtained with the *RVF* method. This shows the good ability of the *SBVF* method to generate optimized virtual displacement fields for hyperelastic behavior.

For the Ogden model, only four loading levels were considered in the identification procedure. They corresponded to an applied

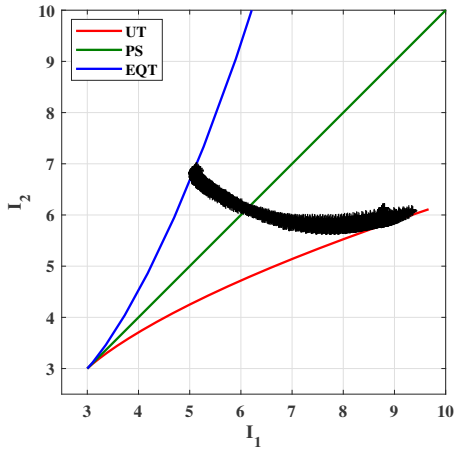

Figure 8 Loading states distributions over the *ROI* for a global stretch $\lambda_{glob} = 2.33$, each point in the graph corresponds to a data point in the *ROI*

Model	Parameter	$x_0 = x_{ref}$	$x_0 = x_{min}$	$x_0 = x_{max}$
Mooney	c_1	$0.229\ MPa$	-	-
	c_2	$9.4\ 10^{-3}\ MPa$	-	-
Ogden 1	μ_1	$0.38\ MPa$	$0.29\ MPa$	$0.36\ MPa$
	α_1	2.39	2.85	2.31
Ogden 2	μ_1	$0.073\ MPa$	$0.378\ MPa$	$0.145\ MPa$
	α_1	2	1.34	2.76
	μ_2	$0.375\ MPa$	$0.24\ MPa$	$0.227\ MPa$
	α_2	1.99	1.34	2.77

Table 3 Identified hyperelastic constitutive parameters using randomly-generated virtual displacement fields

Model	Parameter	Reference	Max	Min
Mooney	c_1	$0.4\ MPa$	$1\ MPa$	$0.1\ MPa$
	c_2	$0.04\ MPa$	$0.1\ MPa$	$0.01\ MPa$
Ogden 1	μ_1	$0.768\ MPa$	$0.84\ MPa$	$0.68\ MPa$
	α_1	1.26	1.63	0.8
Ogden 2	μ_1	$0.114\ MPa$	$0.81\ MPa$	$1.4\ 10^{-4}\ MPa$
	α_1	7.297	11.94	1.58
	μ_2	$0.772\ MPa$	$1.6\ MPa$	$-9.6\ 10^{-3}\ MPa$
	α_2	-0.295	1.31	-7.81

Table 4 Reference values for the constitutive parameters

displacement of 17.5, 35, 52.5 and 70 *mm*. Moreover, the identification was carried out with the fourth loading, for which the Mullins effect was eliminated.

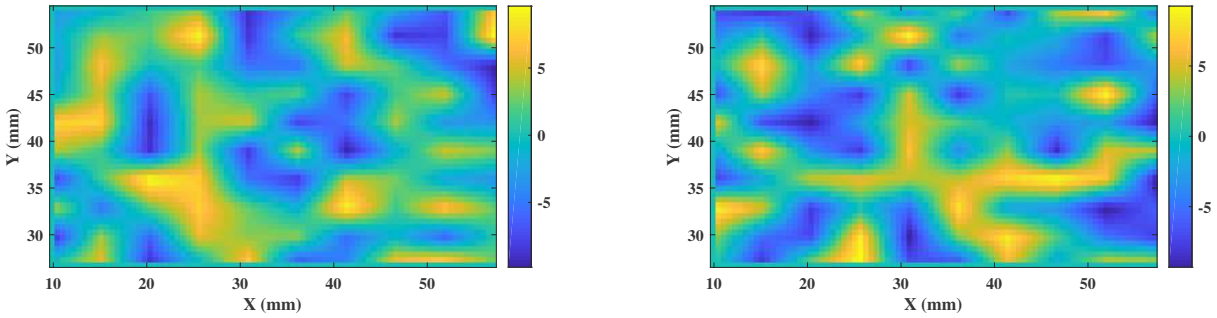

(a) $U_x^{*(1)}$ (mm)

(b) $U_y^{*(1)}$ (mm)

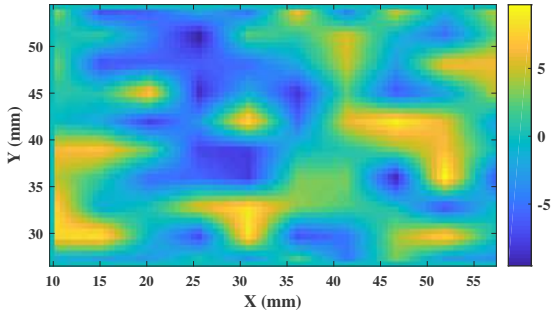

(c) $U_x^{*(2)}$ (mm)

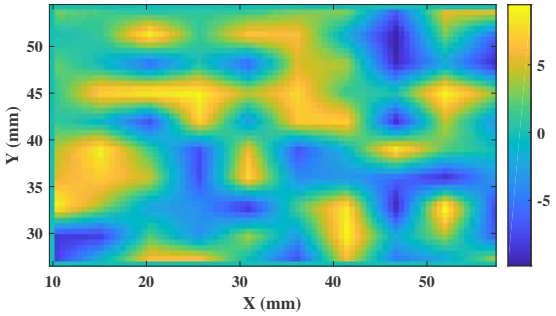

(d) $U_y^{*(2)}$ (mm)

Figure 9 Randomly-generated virtual fields for the identification of the Mooney model

5 | GENERALIZATION CAPABILITY OF THE IDENTIFICATION PROCEDURE

The section aims at evaluating the generalization capability of the proposed methodology by characterizing other hyperelastic materials. In order to illustrate the potential of the methodology, four hyperelastic materials that differ significantly in stiffness and stress hardening have been considered. They are denoted by M1, M2, M3 and M4. As in the previous section, the accuracy of the identified parameters is highlighted the fact that these parameters enable us to correctly predict the force measured during the test. Figure 13 shows these results. It can be concluded that, regardless of the load level obtained with the material and the amount of the stress hardening, the *SBVF* is a well suitable method to generate virtual displacement fields for hyperelastic models

6 | CONCLUSION

In this work, the *VFM* was applied in order to identify the constitutive parameters of two hyperelastic models. Two methods were employed for the generation of the virtual displacement fields. The first method consisted in randomly generating the virtual displacement at all nodes of the correlation grid. Then, the virtual displacement was interpolated around every point using a finite element formulation. The second method is based on the sensitivity of the stress fields to changes of the constitutive parameters. The virtual displacement fields were then computed from the stress sensitivity fields following a finite element formulation. A

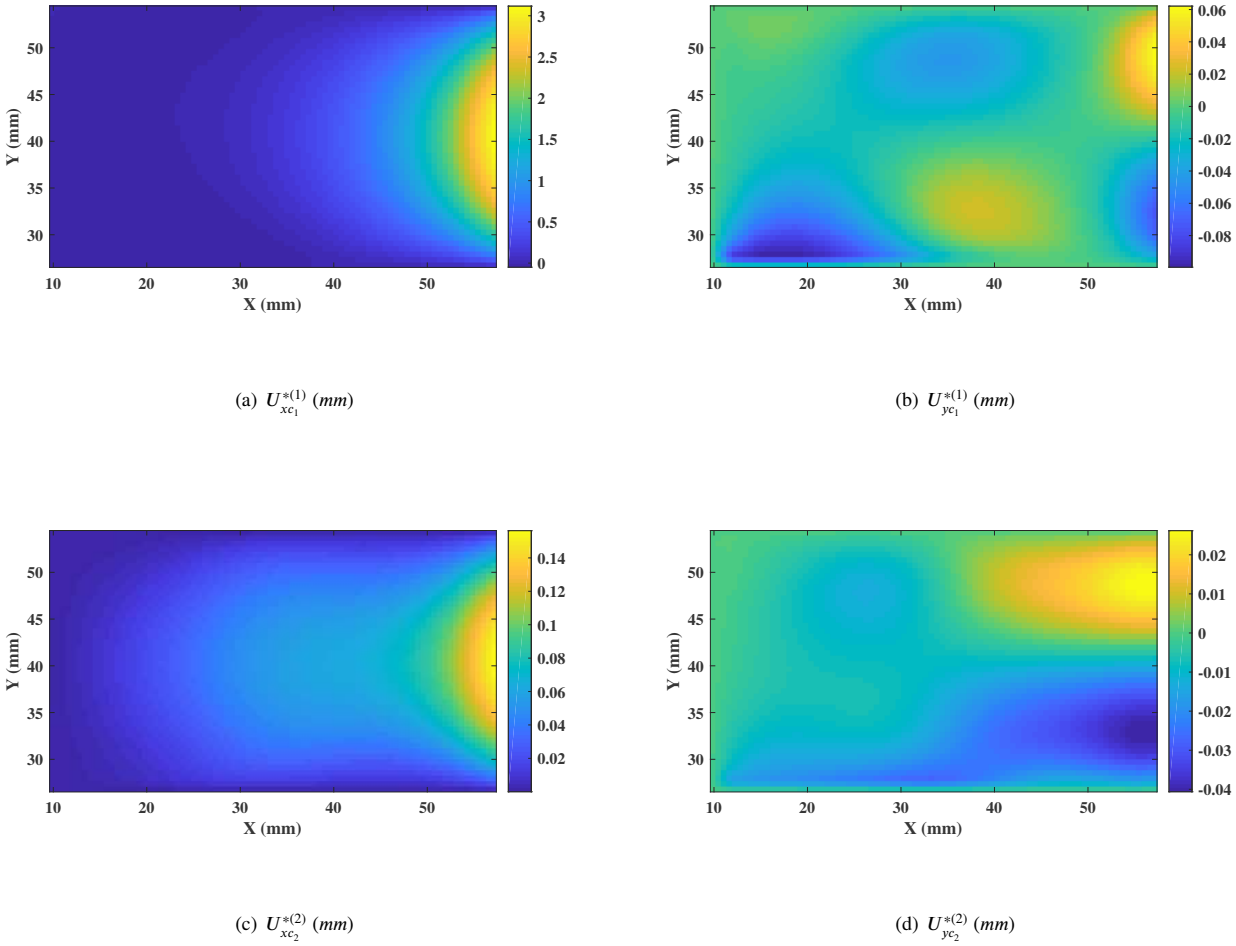

(a) $U^{*(1)}_{xc_1}$ (mm)

(b) $U^{*(1)}_{yc_1}$ (mm)

(c) $U^{*(2)}_{xc_2}$ (mm)

(d) $U^{*(2)}_{yc_2}$ (mm)

Figure 10 Sensitivity-based virtual fields for the identification of the Mooney model

sufficient number of virtual fields was generated to be used in the identification procedure.

Two hyperelastic models were investigated in this work: the Mooney model and two orders of the Ogden model. For the Mooney model, good results were found using both the *RVF* and the *SBVF* methods in the corresponding valid deformation range. Indeed, for both methods, the force in the branch of the cruciform specimen obtained from numerical simulations using identified parameters was very close to the experimental force for a global stretch up to 2. For the Ogden model, the *RVF* method did not give good results for both the first and the second orders. The parameters did not accurately predict the experimental response of the specimen. On the other hand, the parameters obtained from the *SBVF* method were in good agreement with the experimental results in terms of the force in the cruciform branches. Furthermore, the stress hardening phenomenon was well described with the parameters identified for the second-order Ogden model. As in the experiments, the inflection point in the force-displacement curve was found around a global stretch of 2.15. Hence, for a global stretch greater than 2.15, the force-displacement curve slope increases significantly. This feature is very important in the design of rubber component undergoing large deformations in industrial applications. Consequently, for the models considered in this work, the *SBVF* method constitutes a rational procedure for the selection of the virtual fields when applying the *VFM* in the identification of hyperelastic constitutive parameters.

This method could be applied for the identification of other parameters characterizing other physical phenomena observed for rubber materials such as viscoelasticity, Mullins effect or Payne effect. To this end, an adaptation of the method has to be done with respect to the loading conditions as well as the numerical implementation of the method. This will be the subject of future work.

Model	Parameter	Value
Mooney	c_1	0.22 MPa
	c_2	1.9 10^{-2} MPa
Ogden 1	μ_1	0.46 MPa
	α_1	2.11
Ogden 2	μ_1	5.8 10^{-2} MPa
	α_1	3.99
	μ_2	0.5 MPa
	α_2	0.36

Table 5 Parameters identified using sensitivity-based virtual fields

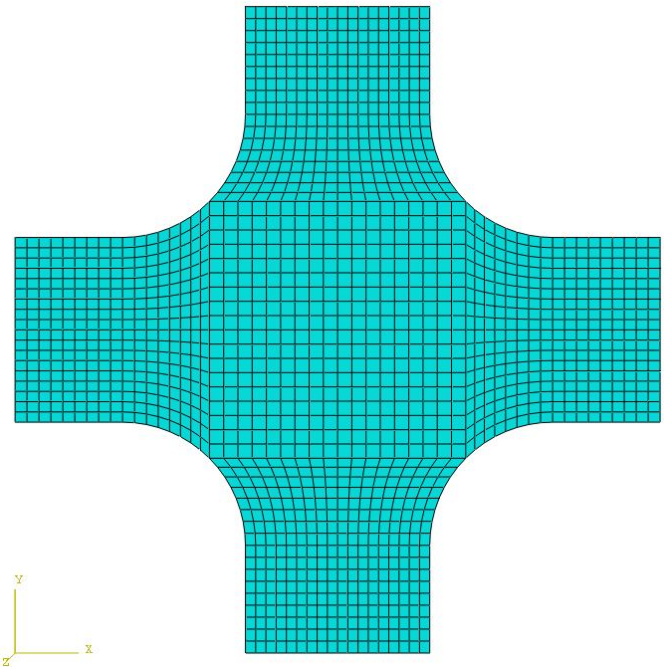

Figure 11 Finite element model for the simulation of the biaxial experiment

ACKNOWLEDGEMENTS

The authors thank M. Marek and Prof. Pierron from Southampton University for providing algorithms dealing with the sensitivity-based virtual fields approach. The authors thank the National Center for Scientific Research (MRCT-CNRS and MI-CNRS), Rennes Metropole and Region Bretagne for financially supporting this work, as well as the Cooper Standard company for providing the specimens.

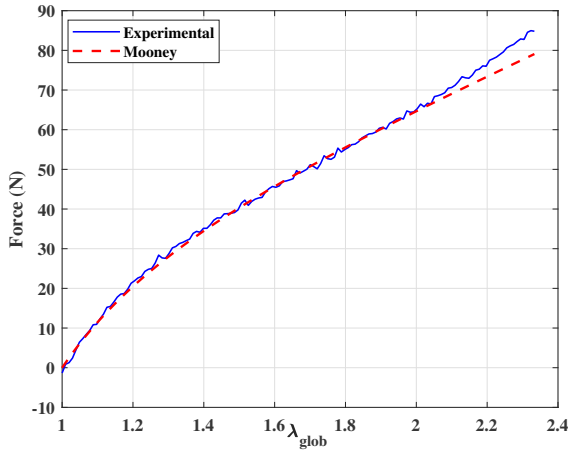

(a) Force obtained with the *RVF* method for the Mooney model

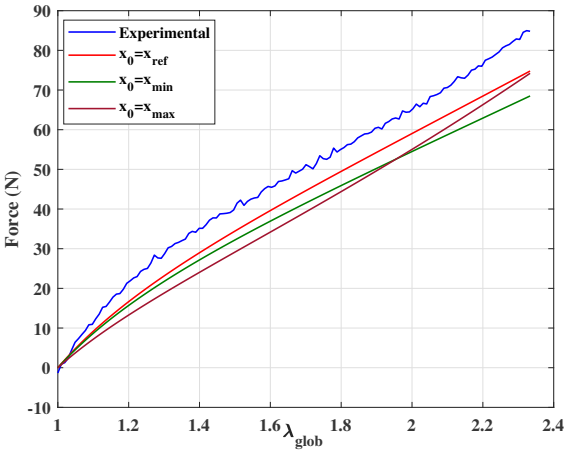

(b) Force obtained with the *RVF* method for the first order Ogden model

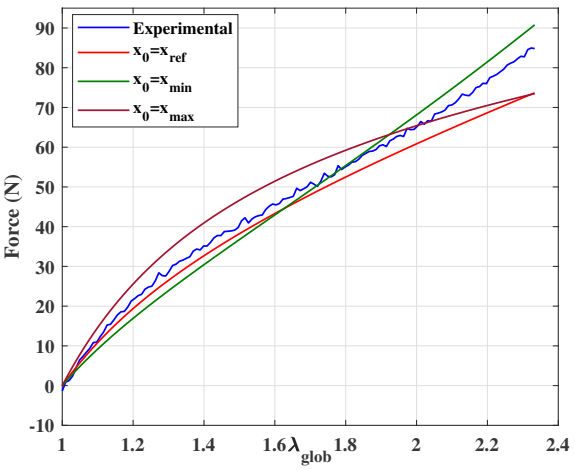

(c) Force obtained with the *RVF* method for the second order Ogden model

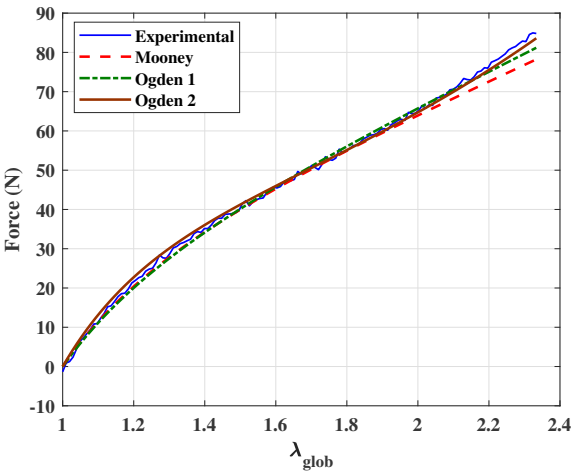

(d) Force obtained with the *SBVF* method

Figure 12 Force obtained from finite element simulations compared to the force force measured during the experiments

APPENDIX

A APPENDIX

Θ is defined as follows:

$$\begin{aligned}
\Theta_{11} &= \frac{2}{D}\left[\left(\lambda_1^2-\lambda_3^2\right)\left(P_{11}^2F_{22}-P_{11}P_{21}F_{12}\right)+\left(\lambda_2^2-\lambda_3^2\right)\left(P_{12}^2F_{22}-P_{12}P_{22}F_{12}\right)\right]\\
\Theta_{12} &= \frac{2}{D}\left[\left(\lambda_1^2-\lambda_3^2\right)\left(-P_{11}^2F_{21}+P_{11}P_{21}F_{11}\right)+\left(\lambda_2^2-\lambda_3^2\right)\left(-P_{12}^2F_{21}+P_{12}P_{22}F_{11}\right)\right]\\
\Theta_{21} &= \frac{2}{D}\left[\left(\lambda_1^2-\lambda_3^2\right)\left(-P_{21}^2F_{12}+P_{11}P_{21}F_{22}\right)+\left(\lambda_2^2-\lambda_3^2\right)\left(-P_{22}^2F_{12}+P_{12}P_{22}F_{22}\right)\right]\\
\Theta_{22} &= \frac{2}{D}\left[\left(\lambda_1^2-\lambda_3^2\right)\left(P_{12}^2F_{11}-P_{11}P_{21}F_{21}\right)+\left(\lambda_2^2-\lambda_3^2\right)\left(P_{22}^2F_{11}-P_{12}P_{22}F_{21}\right)\right]
\end{aligned}, \tag{A1}$$

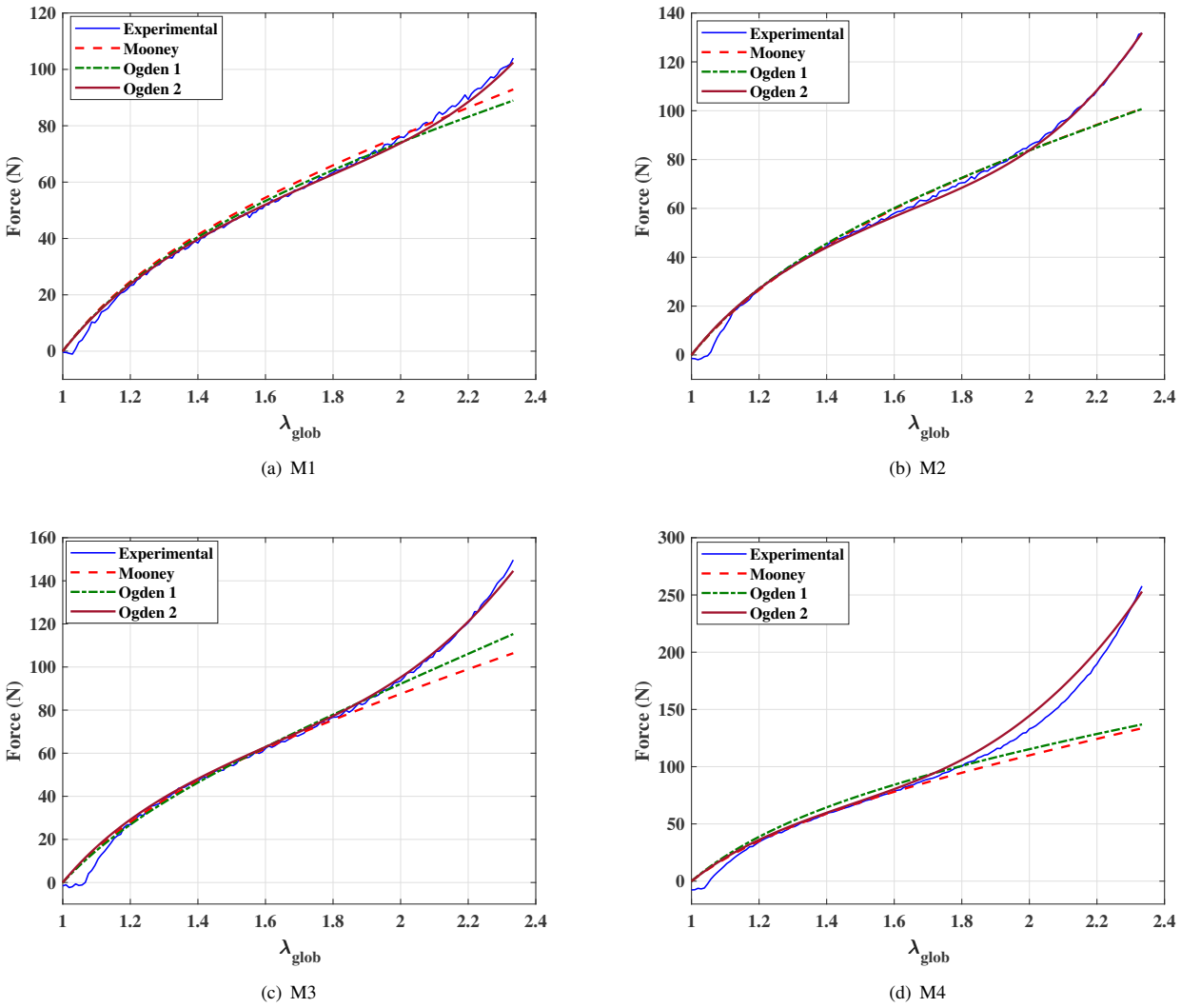

(a) M1 (b) M2

(c) M3 (d) M4

Figure 13 Force obtained from finite element simulations compared to the force measured by considering materials M1, M2, M3 and M4

where $D = F_{11}F_{22} - F_{21}F_{12}$ and $\boldsymbol{P}$ is the transition matrix to the principal stress basis. $\boldsymbol{\Lambda}$ is defined as follows:

$$\begin{aligned}
\Lambda_{11} &= \frac{2}{D}\left[\left(\frac{1}{\lambda_1^2}-\frac{1}{\lambda_3^2}\right)\left(P_{11}^2F_{22}-P_{11}P_{21}F_{12}\right)+\left(\frac{1}{\lambda_2^2}-\frac{1}{\lambda_3^2}\right)\left(P_{12}^2F_{22}-P_{12}P_{22}F_{12}\right)\right]\\
\Lambda_{12} &= \frac{2}{D}\left[\left(\frac{1}{\lambda_1^2}-\frac{1}{\lambda_3^2}\right)\left(-P_{11}^2F_{21}+P_{11}P_{21}F_{11}\right)+\left(\frac{1}{\lambda_2^2}-\frac{1}{\lambda_3^2}\right)\left(-P_{12}^2F_{21}+P_{12}P_{22}F_{11}\right)\right]\\
\Lambda_{21} &= \frac{2}{D}\left[\left(\frac{1}{\lambda_1^2}-\frac{1}{\lambda_3^2}\right)\left(-P_{21}^2F_{12}+P_{11}P_{21}F_{22}\right)+\left(\frac{1}{\lambda_2^2}-\frac{1}{\lambda_3^2}\right)\left(-P_{22}^2F_{12}+P_{12}P_{22}F_{22}\right)\right]\\
\Lambda_{22} &= \frac{2}{D}\left[\left(\frac{1}{\lambda_1^2}-\frac{1}{\lambda_3^2}\right)\left(P_{12}^2F_{11}-P_{11}P_{21}F_{21}\right)+\left(\frac{1}{\lambda_2^2}-\frac{1}{\lambda_3^2}\right)\left(P_{22}^2F_{11}-P_{12}P_{22}F_{21}\right)\right]
\end{aligned}. \tag{A2}$$

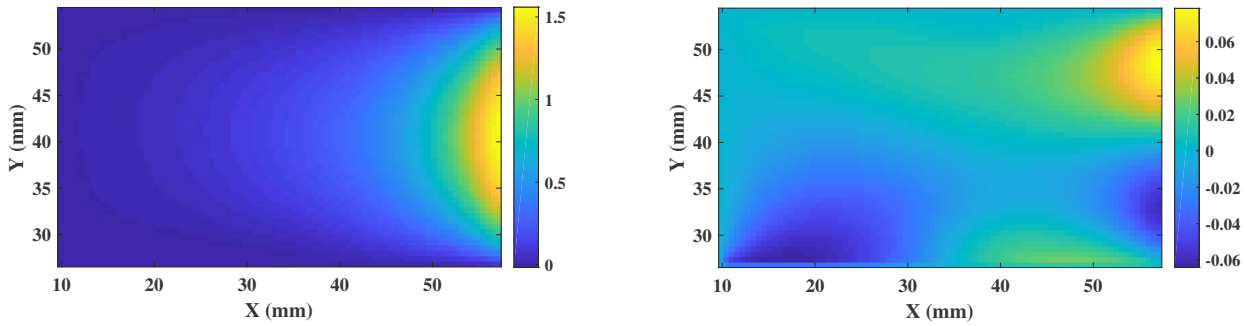

(a) $U^{*(1)}_{x\mu_1}$ (mm) (b) $U^{*(1)}_{y\mu_1}$ (mm)

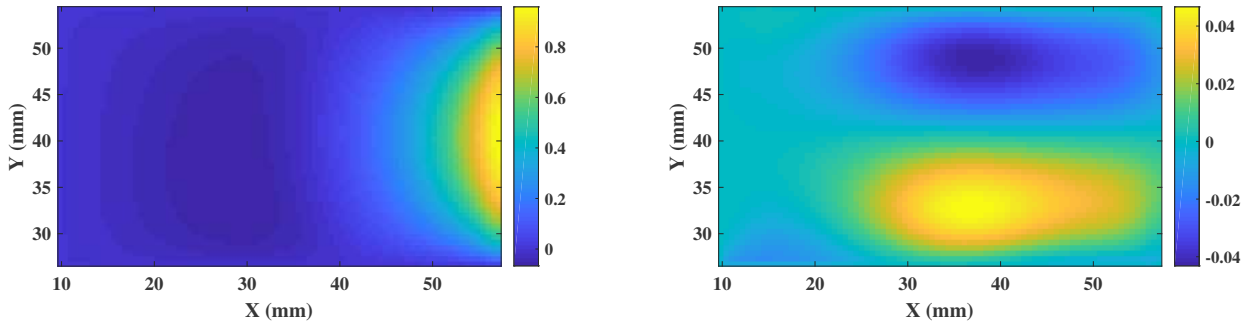

(c) $U^{*(2)}_{x\alpha_1}$ (mm) (d) $U^{*(2)}_{y\alpha_1}$ (mm)

Figure A1 Sensitivity-based virtual displacement fields for the first order Ogden model

References

[1] Avril, S., M. Bonnet, A.-S. Bretelle, M. Grédiac, F. Hild, P. Ienny, F. Latourte, D. Lemosse, S. Pagano, E. Pagnacco, et al., 2008: Overview of identification methods of mechanical parameters based on full-field measurements. *Experimental Mechanics*, **48**, no. 4, 381.

[2] Avril, S. and F. Pierron, 2007: General framework for the identification of constitutive parameters from full-field measurements in linear elasticity. *International Journal of Solids and Structures*, **44**, no. 14-15, 4978–5002.

[3] Avril, S., F. Pierron, Y. Pannier, and R. Rotinat, 2008: Stress reconstruction and constitutive parameter identification in plane-stress elasto-plastic problems using surface measurements of deformation fields. *Experimental Mechanics*, **48**, no. 4, 403–419.

[4] Bornert, M., F. Brémand, P. Doumalin, J.-C. Dupré, M. Fazzini, M. Grediac, F. Hild, S. Mistou, J. Molimard, J.-J. Orteu, et al., 2009: Assessment of digital image correlation measurement errors: methodology and results. *Experimental mechanics*, **49**, no. 3, 353–370.

[5] Chalal, H., S. Avril, F. Pierron, and F. Meraghni, 2006: Experimental identification of a nonlinear model for composites using the grid technique coupled to the virtual fields method. *Composites Part A: Applied Science and Manufacturing*, **37**, no. 2, 315–325.

[6] Giraudeau, A. and F. Pierron, 2003: Simultaneous identification of stiffness and damping properties of isotropic materials from forced vibrating plates. *Comptes Rendus Mécanique*, **331**, no. 4, 259–264.

[7] Grédiac, M. and F. Pierron, 2006: Applying the virtual fields method to the identification of elasto-plastic constitutive parameters. *International Journal of Plasticity*, **22**, no. 4, 602–627.

[8] Grédiac, M., E. Toussaint, and F. Pierron, 2002: Special virtual fields for the direct determination of material parameters with the virtual fields method. 2—-application to in-plane properties. *International Journal of Solids and Structures*, **39**, no. 10, 2707–2730.

[9] Grédiac, M., 1989: Principe des travaux virtuels et identification. *Comptes rendus de l'Académie des sciences. Série 2, Mécanique, Physique, Chimie, Sciences de l'univers, Sciences de la Terre*, **309**, no. 1, 1–5.

[10] Grédiac, M. and F. Pierron, 1998: A t-shaped specimen for the direct characterization of orthotropic materials. *International Journal for Numerical Methods in Engineering*, **41**, no. 2, 293–309.

[11] Grédiac, M., E. Toussaint, and F. Pierron, 2002: Special virtual fields for the direct determination of material parameters with the virtual fields method. 1—-principle and definition. *International Journal of Solids and Structures*, **39**, no. 10, 2691–2705.

[12] Guélon, T., E. Toussaint, J.-B. Le Cam, N. Promma, and M. Grédiac, 2009: A new characterisation method for rubber. *Polymer testing*, **28**, no. 7, 715–723.

[13] Guo, Z. and L. Sluys, 2006: Application of a new constitutive model for the description of rubber-like materials under monotonic loading. *International Journal of Solids and Structures*, **43**, no. 9, 2799–2819.

[14] Holzapfel, G. A., 2002: Nonlinear solid mechanics: a continuum approach for engineering science. *Meccanica*, **37**, no. 4, 489–490.

[15] Jones, E. M., M. A. Iadicola, et al., 2018: A good practices guide for digital image correlation. *International Digital Image Correlation Society*.

[16] Marckmann, G. and E. Verron, 2006: Comparison of hyperelastic models for rubber-like materials. *Rubber chemistry and technology*, **79**, no. 5, 835–858.

[17] Marek, A., F. M. Davis, and F. Pierron, 2017: Sensitivity-based virtual fields for the non-linear virtual fields method. *Computational Mechanics*, **60**, no. 3, 409–431.

[18] Marek, A., F. M. Davis, M. Rossi, and F. Pierron, 2018: Extension of the sensitivity-based virtual fields to large deformation anisotropic plasticity. *International Journal of Material Forming*, 1–20.

[19] Mooney, M., 1940: A theory of large elastic deformation. *Journal of applied physics*, **11**, no. 9, 582–592.

[20] Mullins, L., 1969: Softening of rubber by deformation. *Rubber chemistry and technology*, **42**, no. 1, 339–362.

[21] Ogden, R., G. Saccomandi, and I. Sgura, 2004: Fitting hyperelastic models to experimental data. *Computational Mechanics*, **34**, no. 6, 484–502.

[22] Ogden, R. W., 1972: Large deformation isotropic elasticity–on the correlation of theory and experiment for incompressible rubberlike solids. *Proc. R. Soc. Lond. A*, **326**, no. 1567, 565–584.

[23] Palmieri, G., M. Sasso, G. Chiappini, and D. Amodio, 2011: Virtual fields method on planar tension tests for hyperelastic materials characterisation. *Strain*, **47**, 196–209.

[24] Pierron, F. and M. Grédiac, 2012: *The virtual fields method: extracting constitutive mechanical parameters from full-field deformation measurements*. Springer Science & Business Media.

[25] Promma, N., B. Raka, M. Grédiac, E. Toussaint, J.-B. Le Cam, X. Balandraud, and F. Hild, 2009: Application of the virtual fields method to mechanical characterization of elastomeric materials. *International Journal of Solids and Structures*, **46**, no. 3-4, 698–715.

[26] Sutton, M. A., J. J. Orteu, and H. Schreier, 2009: *Image correlation for shape, motion and deformation measurements: basic concepts, theory and applications*. Springer Science & Business Media.

[27] Toussaint, E., M. Grédiac, and F. Pierron, 2006: The virtual fields method with piecewise virtual fields. *International Journal of Mechanical Sciences*, **48**, no. 3, 256–264.

[28] Treloar, L. R. G., 1975: *The physics of rubber elasticity*. Oxford University Press, USA.

[29] Truesdell, C. and W. Noll, 2004: The non-linear field theories of mechanics. *The non-linear field theories of mechanics*, Springer, 1–579.

[30] Vacher, P., S. Dumoulin, F. Morestin, and S. Mguil-Touchal, 1999: Bidimensional strain measurement using digital images. *Proceedings of the Institution of Mechanical Engineers, Part C: Journal of Mechanical Engineering Science*, **213**, no. 8, 811–817.

[31] Yeoh, O. H., 1993: Some forms of the strain energy function for rubber. *Rubber Chemistry and technology*, **66**, no. 5, 754–771.

[32] Yoon, S.-h. and C. R. Siviour, 2018: Application of the virtual fields method to a relaxation behaviour of rubbers. *Journal of the Mechanics and Physics of Solids*, **116**, 416–431.

[33] Yoon, S.-h., M. Winters, and C. Siviour, 2016: High strain-rate tensile characterization of epdm rubber using non-equilibrium loading and the virtual fields method. *Experimental Mechanics*, **56**, no. 1, 25–35.

[34] Zienkiewicz, O. C., R. L. Taylor, O. C. Zienkiewicz, and R. L. Taylor, 1977: *The finite element method*, volume 36. McGraw-hill London.

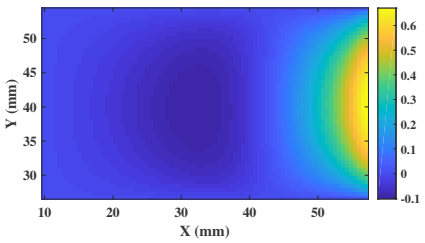

(a) $U^{*(1)}_{x\mu_1}$ (mm)

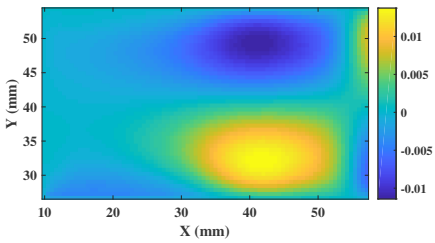

(b) $U^{*(1)}_{y\mu_1}$ (mm)

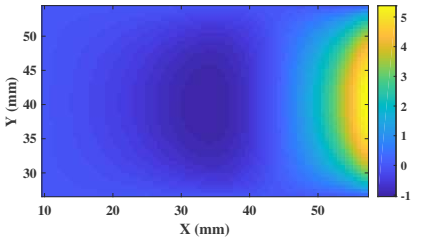

(c) $U^{*(2)}_{x\alpha_1}$ (mm)

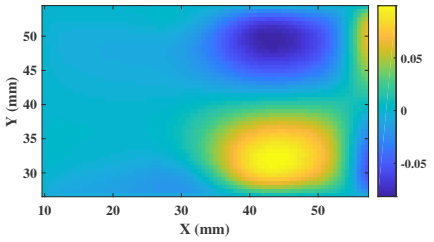

(d) $U^{*(2)}_{y\alpha_1}$ (mm)

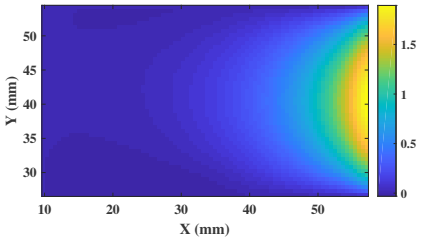

(e) $U^{*(3)}_{x\mu_2}$ (mm)

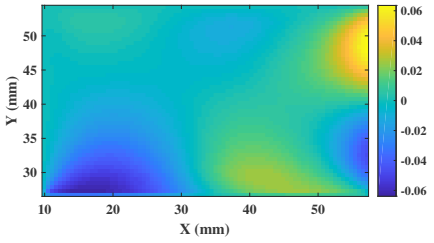

(f) $U^{*(3)}_{y\mu_2}$ (mm)

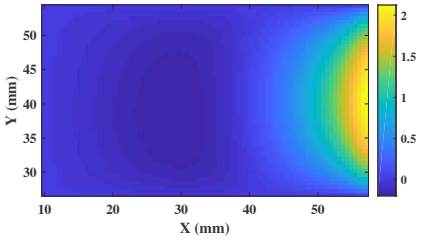

(g) $U^{*(4)}_{x\alpha_2}$ (mm)

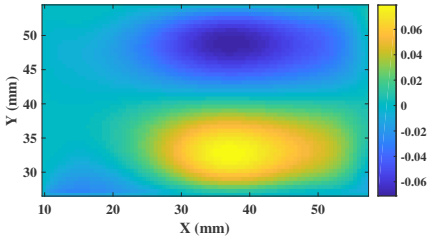

(h) $U^{*(4)}_{y\alpha_2}$ (mm)

Figure A2 Sensitivity-based virtual displacement fields for the second order Ogden model